Supporting Information

Xu et al. 10.1073/pnas.1615733114

Effect of Atmospheric Contamination

To explore the effect of exposing these small-scale Li samples to atmosphere, we placed a representative 4.80-μm-diameter pillar in air for 30 s and then compressed it. Fig. S2*A* shows the yield strength to be ∼200 MPa, after which the sample catastrophically failed, which is approximately four times higher than the ∼50-MPa yield strength of a typical unoxidized Li sample of similar size. The initial loading stiffness is also much higher in the oxidized sample. This is likely due to the immediate formation of LiOH, Li_2O, and Li_3N, which would have greater strength compared with Li. Postcompression image shown in Fig. S2*B* clearly reveals charging of the pillar, consistent with the formation of insulating oxides through a significant portion of the pillar. Under our careful transfer protocol involving the Vacushut device, the surface contamination is kept to a minimum to the point that it does not significantly influence the mechanical properties of the pillars. This can be seen from the elastic modulus values we obtained from our unloading data. Based on our calculations, the expected range for the elastic modulus is 3–21.1 GPa, and the average elastic modulus obtained from our unloading data, across all pillar sizes, is 5.28 GPa. We found the average elastic modulus of pillars with diameters below 2 μm to be 5.48 GPa, and that for the samples with diameters larger than 4 μm is 5.15 GPa. This suggests that the average elastic modulus that we measured remains virtually equivalent for small and large pillars.

Identifying the Crystal Orientation of Pillars

After compression, we transferred the Li sample to another SEM (Zeiss; 1550VP FESEM) to determine the crystallographic orientations of each pillar using electron backscatter diffraction (EBSD). This was done postcompression because the Vacushut is not compatible with the Zeiss SEM, and therefore the sample must be removed from the Vacushut and temporarily exposed to air before doing EBSD. From the previous discussion, we know that exposing Li to atmosphere even for 30 s caused significant oxidation, and therefore identifying the crystal orientation before the fabrication of pillars using FIB is not an option. We show the grain structure of melted and then subsequently cooled down Li metal in Fig. S3 *A* and *B*. EBSD was conducted on a blade-cut surface showing a mirror finish. Chemical polishing has been unsuccessful in further smoothing the surface. Nash and Smith (42) found that methanol was the best etchant for Li metal, and that repeated actions of etching in methanol for a few seconds, and then rinsing in xylene, would allow for visual observation of grain boundaries. However, this process must be done in the open air. If the same procedure was followed in an Ar atmosphere, a white crust forms on the surface of Li as soon it is removed from methanol. This is exactly what we have found in our studies. Ethanol and isopropanol was also used to no avail. Preparation of Li metal outside the glovebox, although it may allow for visual observation of grain boundaries, introduces an oxide layer that makes it impossible to characterize the underlying Li using EBSD. Therefore, EBSD was conducted on an as-cut lithium metal surface, where the roughness prohibited indexing of certain regions. Regardless, the indexed points are sufficient in indicating the average grain size of our lithium sample, around 250 ± 86 μm, as shown in Fig. S3 *A* and *B*. The fact that our pillars, with diameters less than 10 μm, are much smaller than the average grain size leads us to conclude that our pillars are single crystalline. This assumption is often used in the nanomechanical community when studying polycrystalline material (43). An instance of this is shown in Fig. S3*C*. In some instances, however, it is difficult to identify which particular grain the pillars belong to, as shown in Fig. S3*D*. In these cases, to obtain the crystal orientation of pillars to calculate the Schmidt factor, we used the relation between the elastic modulus of a particular grain and its Miller indices as given below (44):

$$\frac{1}{E_{hkl}} = s_{11} - 2\left(s_{11} - s_{12} - \frac{1}{2}s_{44}\right)\cdot\frac{h^2k^2 + h^2l^2 + k^2l^2}{\left(h^2 + k^2 + l^2\right)^2}, \qquad \textbf{[S1]}$$

where h, k, and l are the miller indices of the respective grain; S_{11}, S_{12}, and S_{44} are the elements of the compliance matrix; and E_{hkl} is the orientation-dependent elastic modulus. E_{hkl} is obtained from the uniaxial compliance measured from unloading. The top one-third of the unloading curve, starting at the point of maximum depth, is linearly fitted and the slope is taken to be E. Elements of the compliance matrix are calculated from the elastic constants (17, 18, 42). The symmetry of Eq. **S1** prevents us from uniquely identifying the exact sequence and sign of the h, k, and l values; however, the maximum Schmidt factor is the same for every permutation.

Effect of Ga^+ Implantation

Indentations are performed on FIB'd and as-cut Li surfaces. Ion beam with a 30-nA current was used to polish the surface of as-cut Li at a grazing angle. We performed nanoindentations to a depth of up to 3 μm to match the deforming indentation volume to that of the pillars. The load vs. displacement data are for the FIB-polished and as-cleaved Li surfaces is shown in Fig. S4 and reveals that these surface treatments lead to statistically indistinguishable mechanical properties. These results are consistent with multiple previous reports, which demonstrated that FIB irradiation did not significantly affect the strength and deformation of metallic micropillars and nanopillars (34, 45).

Calculating the Average Shear Modulus of a Single Crystal

Turley and Sines (46) gave the general expression for the shear modulus of a single crystal below:

$$G = \frac{1}{s_{44} + 4\left(s_{11} - s_{12} - \frac{1}{2}s_{44}\right)\Omega}, \qquad \textbf{[S2]}$$

where s_{11}, s_{12}, and s_{44} are elements of the compliance matrix, and Ω is the angle dependence as defined below:

$$\Omega = a + b\sin 2\theta + c\cos 2\theta, \qquad \textbf{[S3]}$$

where a, b, and c are linear combinations of the directional cosines of (hkl). It is clear that when Eq. **S3** is averaged over 2π with respect to Θ, the sinusoidal terms disappear. The expression for a is given as follows:

$$a = A^2B^2 + C^2D^2, \qquad \textbf{[S4]}$$

where

$$\begin{aligned} A &= \cos\alpha\cos\beta \\ B &= \sin\alpha\cos\beta \\ C &= \sin\beta \\ D &= \cos\beta, \end{aligned} \qquad \textbf{[S5]}$$

and

$$\sin\alpha=\frac{k}{(h^2+k^2)^{1/2}};\quad \sin\beta=\frac{l}{(h^2+k^2+l^2)^{1/2}}$$
$$\cos\alpha=\frac{h}{(h^2+k^2)^{1/2}};\quad \cos\beta=\left(\frac{h^2+k^2}{h^2+k^2+l^2}\right)^{1/2}. \qquad [S6]$$

A schematic is provided in Fig. S5.

Density Functional Theory Calculations

The lattice constant at each temperature was calculated by free-energy minimization and the vibrational contribution to free energy was calculated at each of the temperatures using the method described below.

We express the free energy F in terms of the strain state at a constant volume as follows (47, 48):

$$F=F_0+\frac{V}{2}\sum_{i=1}^{6}\sum_{j=1}^{6}C_{ij}e_ie_j+O\left(e_i^3\right), \qquad [S7]$$

where F_0 denotes the free energy at zero strain. We used volume-conserving orthorhombic strain and monoclinic strains for cubic crystals (47). The volume-conserving orthorhombic strain is given by the following:

$$\begin{aligned}&e_1=-e_2=x,\\&e_3=\frac{x^2}{1-x^2}\\&e_4=e_5=e_6=0.\end{aligned} \qquad [S8]$$

In this case, the free-energy change is an even function of the strain and is given by the following:

$$F=F_0+V(C_{11}-C_{12})x^2+O\left(x^4\right). \qquad [S9]$$

This allows the determination of the elastic constant $C_{11}-C_{12}$. In a similar fashion, volume-conserving monoclinic strain is given by the following:

$$\begin{aligned}&e_6=x\\&e_3=\frac{x^2}{4-x^2}\\&e_1=e_2=e_4=e_5=0.\end{aligned} \qquad [S10]$$

In this case, the resulting free-energy change is again an even function of the strain given by the following:

$$F=F_0+\frac{V}{2}C_{44}x^2+O\left(x^4\right). \qquad [S11]$$

This allows us to calculate the elastic constant C_{44}.

To isolate the individual elastic constants, C_{11} and C_{12}, we used the relationship $B=(C_{11}+2C_{12})/3$, where B is the bulk modulus, calculated by fitting Birch–Murnaghan equation of state to the free-energy variation with volume obtained from the density functional theory calculations (49).

We account for the free-energy contribution due to lattice vibrations using the quasiharmonic approximation, where the total free energy for a cubic crystal can be written as follows (35, 50):

$$F(V,T)=E(V)-k_BT\ln Z(V,T), \qquad [S12]$$

where E is the energy of the frozen lattice at volume V, k_B is the Boltzmann constant, and Z is the partition function associated with the vibrations at temperature T (35). We consider only the phonon vibrational contributions, which can be expressed in terms of the phonon vibrational frequencies ω and density of states $g(\omega,V)$, given by the following:

$$Z(V,T)=\int_0^\infty g(\omega,V)\ln\frac{1}{2\sinh\left(\frac{\hbar\omega}{k_BT}\right)}d\omega. \qquad [S13]$$

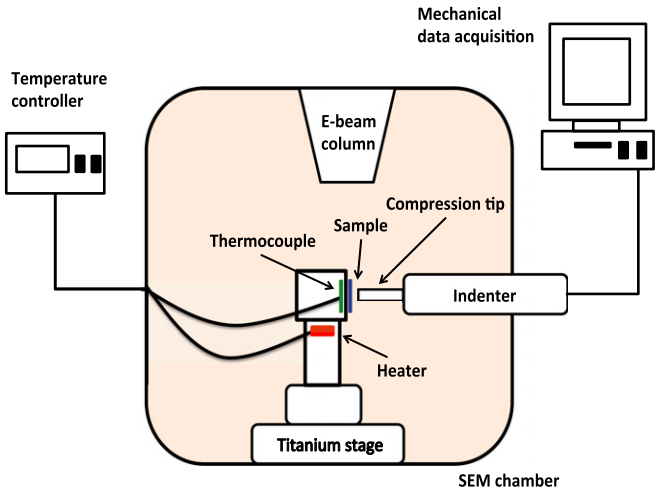

Fig. S1. Schematic of SEMentor. Based on Lee et al. (22). Modifications were made to his original system to achieve above room temperature testing.

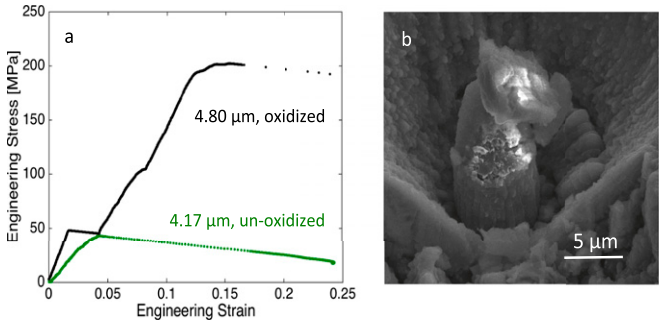

Fig. S2. Compression results of oxidized an unoxidized pillar. (*A*) Engineering stress vs. engineering strain data of the compression of a 4.8-μm oxidized pillar, comparing with the data of a 4.17-μm unoxidized pillar. The first strain burst during loading is due to cracks formed via oxidation. (*B*) Postcompression image of the oxidized pillar. White parts due to the charging effective of nonconductive material.

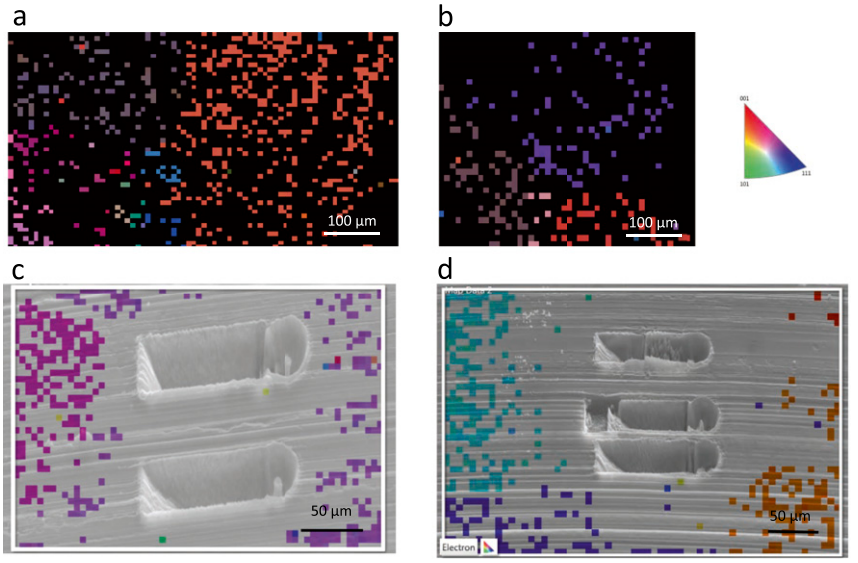

Fig. S3. Crystal grain map of Li substrate with pillars postcompression. (*A* and *B*) Orientation imaging microscopy map generated by EBSD showing the annealed and as-cut surface of the Li sample, with grain size 250 ± 86 μm. (*C* and *D*) SEM image of pillars postcompression overlaid with orientation mapping.

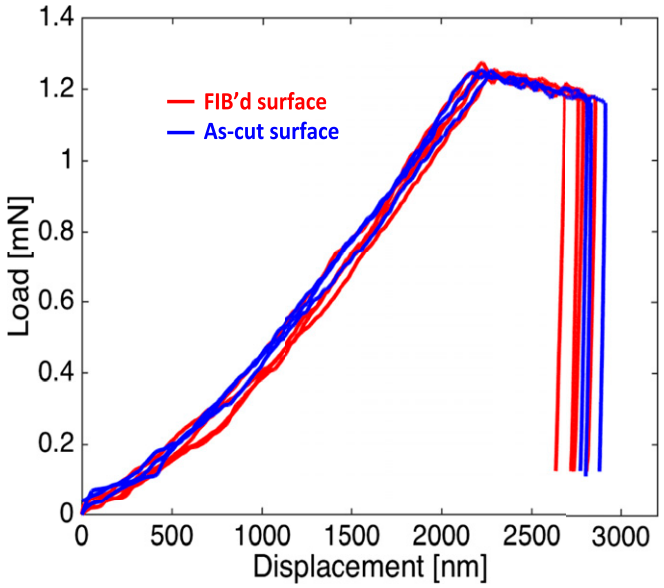

Fig. S4. Load-controlled indentation of Li metal with a cleaved surface (red) and FIB-polished surface (blue). The conditions for the FIB are 30-keV acceleration voltage and 30-nA current.

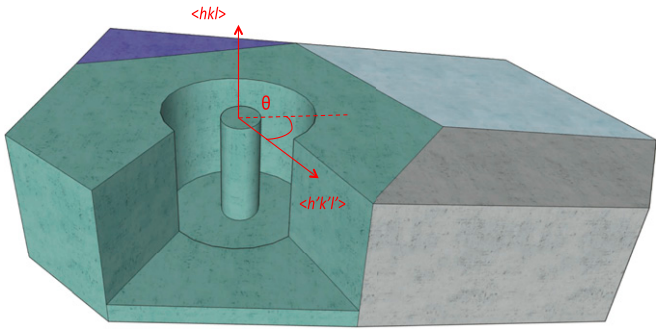

Fig. S5. A single-crystalline pillar situated within a crystal grain with normal in the direction of <*hkl*>. The different colored regions indicate different crystal grains imbedded in a polycrystalline Li metal foil. <*h*′*k*′*l*′> is a transverse direction in the (*hkl*) plane. Θ is the angle between <*h*′*k*′*l*′> and the meridional tangent (indicated by the dashed line). For the definition, please refer to Turley and Sines (46).

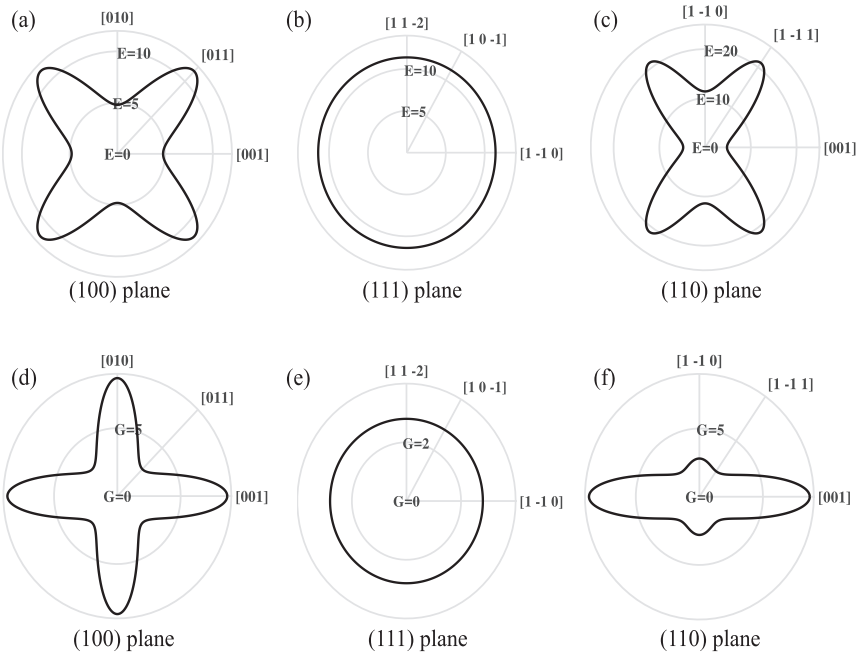

Fig. S6. In-plane directional dependence of the elastic modulus of Li in (100) plane (*A*), (111) plane (*B*), and (110) plane (*C*). The same dependence is plotted for the shear modulus in (100) plane (*D*), (111) plane (*E*), and (110) plane (*F*).